

Article

Protonation State of an Important Histidine from High Resolution Structures of Lytic Polysaccharide Monoxygenases

Sanchari Banerjee ¹, Sebastian J. Muderspach ¹, Tobias Tandrup ¹, Kristian Erik Høpfner Frandsen ^{1,2}, Raushan K. Singh ¹, Johan Ørskov Ipsen ^{2,3}, Cristina Hernández-Rollán ⁴, Morten H. H. Nørholm ⁴, Morten J. Bjerrum ¹, Katja Salomon Johansen ³ and Leila Lo Leggio ^{1,*}

¹ Department of Chemistry, University of Copenhagen, Universitetsparken 5, DK-2100 Copenhagen, Denmark; saba@chem.ku.dk (S.B.); sjm@chem.ku.dk (S.J.M.); tandrup@chem.ku.dk (T.T.); kehf@plen.ku.dk (K.E.H.F.); singhraushank@gmail.com (R.K.S.); mobj@chem.ku.dk (M.J.B.)

² Department of Plant & Environmental Sciences, University of Copenhagen, Thorvaldsensvej 40, Frederiksberg C, DK-1871 Copenhagen, Denmark; jip@ign.ku.dk

³ Department of Geoscience & Natural Resource Management, University of Copenhagen, Frederiksberg 5, DK-1958 Copenhagen, Denmark; ksj@ign.ku.dk

⁴ The Novo Nordisk Foundation Center for Biosustainability, Technical University of Denmark, Kemitorvet Building 220, DK-2800 Kongens Lyngby, Denmark; crirol@biosustain.dtu.dk (C.H.-R.); morno@biosustain.dtu.dk (M.H.H.N.)

* Correspondence: leila@chem.ku.dk



Citation: Banerjee, S.; Muderspach, S.J.; Tandrup, T.; Frandsen, K.E.H.; Singh, R.K.; Ipsen, J.Ø.; Hernández-Rollán, C.; Nørholm, M.H.H.; Bjerrum, M.J.; Johansen, K.S.; et al. Protonation State of an Important Histidine from High Resolution Structures of Lytic Polysaccharide Monoxygenases. *Biomolecules* **2022**, *12*, 194. <https://doi.org/10.3390/biom12020194>

Academic Editor: Vladimír N. Uversky

Received: 22 November 2021

Accepted: 15 January 2022

Published: 24 January 2022

Publisher's Note: MDPI stays neutral with regard to jurisdictional claims in published maps and institutional affiliations.



Copyright: © 2022 by the authors. Licensee MDPI, Basel, Switzerland. This article is an open access article distributed under the terms and conditions of the Creative Commons Attribution (CC BY) license (<https://creativecommons.org/licenses/by/4.0/>).

Abstract: Lytic Polysaccharide Monoxygenases (LPMOs) oxidatively cleave recalcitrant polysaccharides. The mechanism involves (i) reduction of the Cu, (ii) polysaccharide binding, (iii) binding of different oxygen species, and (iv) glycosidic bond cleavage. However, the complete mechanism is poorly understood and may vary across different families and even within the same family. Here, we have investigated the protonation state of a secondary co-ordination sphere histidine, conserved across AA9 family LPMOs that has previously been proposed to be a potential proton donor. Partial unrestrained refinement of newly obtained higher resolution data for two AA9 LPMOs and re-refinement of four additional data sets deposited in the PDB were carried out, where the His was refined without restraints, followed by measurements of the His ring geometrical parameters. This allowed reliable assignment of the protonation state, as also validated by following the same procedure for the His brace, for which the protonation state is predictable. The study shows that this histidine is generally singly protonated at the Nε2 atom, which is close to the oxygen species binding site. Our results indicate robustness of the method. In view of this and other emerging evidence, a role as proton donor during catalysis is unlikely for this His.

Keywords: polysaccharide monoxygenase; protonation; stereochemical properties; partial unrestrained refinement; auxiliary activities

1. Introduction

Lytic Polysaccharide Monoxygenases (LPMOs) are a recently discovered group of copper metalloenzymes that depolymerize recalcitrant polysaccharides like lignocellulose and chitin by oxidative cleavage of the glycosidic bonds. LPMOs have been shown to boost the activities of other carbohydrate active enzymes, breaking down large crystalline/insoluble polysaccharides into glucans [1–3]. These sugars can then be fermented to bioethanol, a renewable form of energy [4]. This finding sparked the interest in LPMOs as it is a key step in boosting the production of biofuels from the plant biomass [5,6]. Extensive research is being carried out to understand the mechanism of the LPMO catalysis for effective industrial applications [7]. The presence of LPMOs or predicted LPMO-encoding genes has been established in many organisms, including microbes, fungi, algae, plants and insects [7]. Although their complete role in all the organisms is far from understood,

some of the recent studies indicate biological roles of LPMOs in pathogenesis in plants [8,9] and human [10].

LPMOs are classified as Auxiliary Activities (AAs) in the Carbohydrate Active Enzymes database, CAZy.org [11]. They have been extensively reviewed in [12–16]. There are eight families that are categorized as LPMOs: AA9, AA10, AA11, AA13, AA14, AA15, AA16, and AA17 (very recently discovered) [17]. There is a large diversity observed in the origin, substrate specificity, binding and cleavage reactions amongst the different LPMOs. Although the primary amino acid sequence of LPMOs is minimally conserved between families, the active site of the enzyme comprised of the Histidine brace (His-brace) is highly conserved across all LPMOs. The His-brace is made up of the Cu metal center coordinated with the imidazole ring N δ 1 and backbone N atoms of the terminal His and the imidazole ring nitrogen N ϵ 2 atom of a His located later in the protein sequence. In AA9 and several other LPMOs, the Cu is also coordinated with a Tyr at an axial position and two water molecules: one axial (above the Tyr residue) and one equatorial (in the same plane as the two His residues) [18]. These residues constitute the primary co-ordination sphere of the enzyme. Figure 1 shows the active site of AA9A LPMO from *Lentinus similis* (*LsAA9A*) bound to the oligosaccharide cellotriose. Due to the oligosaccharide binding, the axial water is displaced and a chloride ion binds from the crystallization condition at the position of the equatorial water. The active site is on a relatively flat surface site of the enzyme, which facilitates binding to large insoluble/crystalline substrates. This positioning eases the degradation process of the polysaccharides by the LPMOs as the large substrates do not need to enter binding pockets for enzyme activity. The structure of LPMOs from all families determined so far belong to the immunoglobulin G-like β -sandwich fold [19].

The general scheme of the activity of an LPMO is known; however, the full molecular mechanism is still elusive. A simplified diagrammatic representation of the putative mechanism for the oxidative cleavage of a substrate by an LPMO is shown in Figure 2. The reaction is initiated by the reduction of Cu(II) to Cu(I). Some of the electron donors aiding in reduction are (i) chemicals like ascorbic acid [16,20], (ii) the enzyme cellobiose dehydrogenase [21,22], and (iii) lignin from biomass [23]. A higher polysaccharide affinity for the reduced Cu(I) form of some LPMOs could suggest that reduction occurs before binding of the substrate [24]. After reduction and substrate binding, the oxygen species is bound at the equatorial position of the active site of the enzyme. The black arrow in Figure 1 (pointing to the chloride ion) denotes the position of the oxygen-species binding site. The oxygen species could be provided by either molecular O₂ or H₂O₂, although the support for the latter is increasing [25–28]. After binding, the oxygen species is positioned appropriately near the substrate by the residues around the active site. This is likely followed by hydrogen abstraction from the substrate, hydroxylation and elimination of water, resulting in oxidation at either C1 or C4 atoms. However, recent detailed work on *LsAA9A* shows that while glycosidic bond cleavage is dependent on H₂O₂, O₂ is necessary for the production of oxidated oligosaccharides [28]. This suggests that rather than a strict preference for either co-substrates, at least some LPMOs follow more complicated reaction schemes where interactions between metal, oxygen species, protein and reductant determine the final outcome, which is highly sensitive to the reaction conditions.

The 1st and 2nd coordination spheres of transition metal complexes affect the structure and function of the metalloproteins [29]. While the residues of the 1st coordination sphere are mainly involved in bonding, the residues of the 2nd coordination sphere carry out their function via non-covalent interactions. Therefore, as in other transition metal complexes [29,30], the 2nd coordination sphere plays an important role in LPMO activity. 2nd sphere residues have been proposed to facilitate oxygen binding, proton transfer, and stabilization of intermediates through steric, electrostatic, and, especially, H-bonding interactions [27,29–33]. Due to very low sequence conservation across different LPMO families, there are different residues in the secondary coordination sphere that aid in the above reaction mechanism. In this study, the focus is on AA9 LPMOs, where a conserved His and Gln (His147 and Gln162 in *LsAA9A*, Figure 1) form the 2nd coordination sphere and a strong H-bonding network has been shown in the crystal structures [34,35]. Of particular interest is the conserved His residue which has

been shown by mutagenesis to be important for activity in an AA9 LPMO [31]. In addition to a role in positioning the oxygen species correctly along with the conserved Gln in AA9 LPMOs [27,31–33], a role has been discussed as a potential proton donor to the bound oxygen species [27,31–33] during the oxidation of the polysaccharides.

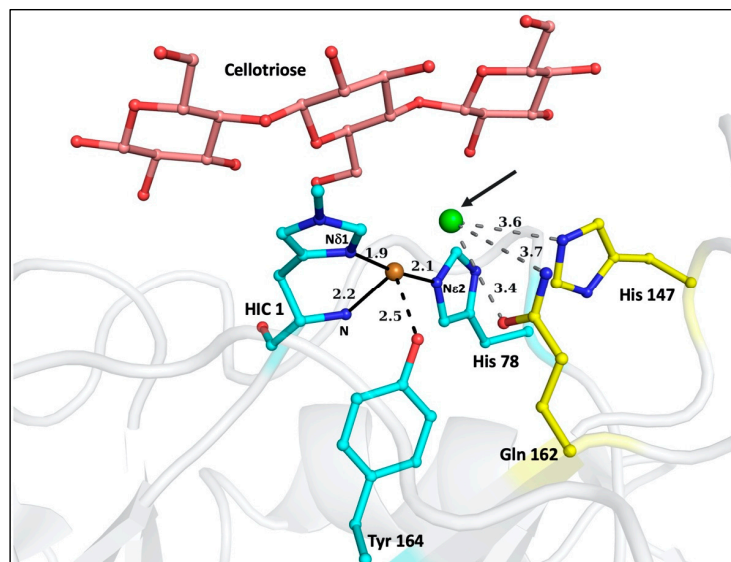


Figure 1. Structure of *Lentinus similis* AA9A (*LsAA9A*), PDB ID: 5ACF showing its active site with the bound oligosaccharide cellotriose. The 1st coordination sphere of the copper (orange sphere) is formed by the residues His1, His78, and Tyr 164 (colored in cyan). The coordination distances are shown in Å. As the oligosaccharide is bound, the axial water is displaced in this structure, but is visible in Figure 4. At the equatorial position, chloride (green sphere) is bound instead of water. This position (pointed with a black arrow) is the presumed binding site for the activated oxygen species. The 2nd coordination sphere residues are His147 and Gln162 (colored in yellow). His147 is conserved across all AA9 LPMOs. The distances from His147 and Gln162 to the chloride in Å are shown in grey. The residues are represented in ball and stick representation. The figure was prepared in Pymol.

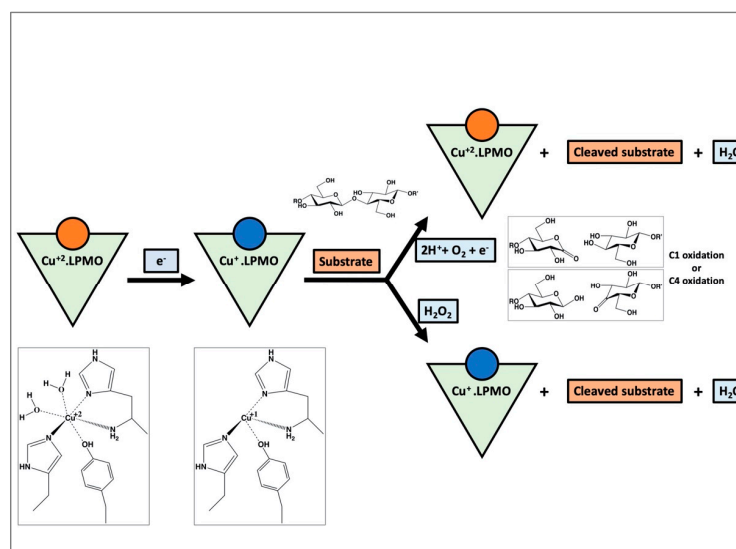


Figure 2. A simplified diagrammatic representation of the reaction mechanism of LPMOs exemplified by cellulose degradation. The reaction proceeds by reduction of the Cu from Cu(II) to Cu(I), substrate binding and the subsequent cleavage of the substrate by the oxygen species. Depending on the source of the oxygen species being either molecular oxygen or hydrogen peroxide, the reaction proceeds differently, yielding the cleaved substrate by C1 or C4 oxidation or both.

Based on quantum mechanics/molecular mechanics (QM/MM calculations), Hedegård and Ryde investigated the effect of protonation state of His147 in *LsAA9A* with a different co-substrate (O_2 or H_2O_2) [27]. With O_2 , a double protonated His seems to be required as proton donor [27,31,32]. On the contrary, if the co-substrate is H_2O_2 , the main role of His147 is the positioning of the co-substrate and not proton transfer, and a singly protonated His is sufficient [27]. Another study [33] shows that the process of O-O bond cleavage along with proton transfer from this double protonated His to oxygen is kinetically unfavorable [33]. Regardless which specific mechanism one wishes to investigate now or in the future, the protonation state of this secondary sphere residue is likely to affect the energy barriers obtained in QM/MM studies and is thus important to consider.

Determining protonation states of residues in proteins experimentally is difficult. Nuclear Magnetic Resonance (NMR) spectroscopy titration and Neutron crystallography are the two most reliable methods [36–40]. While NMR is mostly amenable for small proteins, neutron crystallography is limited by low flux of neutron sources and size of the crystal, among others [41]. Several structures of LPMOs have been determined by NMR [42,43], but protonation states of key residues have not been specifically investigated with it. Neutron crystallography, on the contrary, has been used to investigate the protonation state of the His of the second co-ordination sphere in an AA9 from *Neurospora crassa*. Here the authors demonstrate that this His is singly protonated at N ϵ 2 atom of the imidazole ring [32], but consider also the possibility that the active enzyme may be doubly protonated at low pH~5.0 and take part in proton transfer as the N ϵ 2 atom is located near the O_2 binding site.

In the present study we investigate the protonation state of this His residue using X-ray crystallographic data sets at resolutions better than 1.1 Å using partially unrestrained refinement as previously suggested [44]. Three structures of AA9 from *LsAA9A* and *Thermoascus aurantiacus* (*TaAA9A*) were determined in this study. Additionally we used the same protocol for re-refinement of four structures already deposited in the PDB. Although the secondary sphere His residue is not generally conserved in other families, AA10 LPMO from *Micromonospora aurantiaca* for which a high resolution X-ray crystal structure is available in the PDB [45], is an exception and thus is also included in the analysis. In order to validate the method, we have also used the same protocol to determine the (known) protonation state of the His in the His brace in these structures. The validation results show the robustness of our method for this study. Our results reveal that the conserved His residue of the 2nd coordination sphere in AA9 LPMOs is generally singly protonated.

2. Materials and Methods

2.1. Crystallization

LsAA9A was heterologously produced in *Escherichia coli* (*LsAA9A_Ec*) using the LyGo platform [46]. The protein was purified using Q-Sepharose anion-exchange chromatography and Superdex 75pg size exclusion chromatography and finally concentrated to 13.8 mg/mL in the buffer: 20 mM Na-Acetate pH 5.5 and 150 mM NaCl. It was then incubated with Cu(II) acetate at equimolar ratio for 1 h before crystallization setup. The crystals for *LsAA9A_Ec* were grown in a 24-well VDX plate by the hanging drop vapor diffusion method using 2 μ L each of the protein and the crystallization condition, 0.1 M citric acid pH 3.5 and 3.0 M NaCl. The crystals were cryo-cooled in liquid nitrogen and data were collected at cryogenic temperature (100 K).

TaAA9A was saturated with Cu(I) chloride under anaerobic environment. The filtered *TaAA9A* preparation was then purified as described in [47]. The elution fractions corresponding to *TaAA9A* were pooled and concentrated using an Amicon Ultra-15 centrifugal filter (3 kDa, Merck Millipore Ltd. Darmstadt, Germany). The concentrated *TaAA9A* was again saturated with Cu(I) chloride under anaerobic environment and purified as described above. Finally, the Cu-loaded *TaAA9A* was buffer exchanged in 20 mM MES pH 6.0 and concentrated to 26 mg/mL. The protein sample was then deglycosylated with ~0.05 units per mg *TaAA9A* of endoglycosidase H (Roche Diagnostics A/S Hvidovre, Denmark). The final concentration of the protein was about 20.5 mg/mL in 20 mM MES pH 6.0, 125 mM

NaCl. The protein sample was additionally incubated for 1 h with equimolar concentration of Cu(II) acetate prior to crystallization setup. The crystals of *TaAA9A* were grown at room temperature using the sitting drop vapor diffusion method in MRC two-drop plates set up by an ORYX8 robot. These drops were composed of 0.3 μ L of the protein sample *TaAA9A* and 0.1 μ L of the crystallization condition 0.1 M HEPES pH 7.5, 20 mM $MgCl_2$ and 22 % (*w/v*) polyacrylic acid 5100 sodium salt. All the crystals were flash frozen in liquid nitrogen and data were collected at cryogenic temperature (100 K).

2.2. X-ray Data Collection and Structure Determination

High resolution X-ray diffraction data for *LsAA9A_Ec* and *TaAA9A* crystals were collected at the BioMAX beamline MAX IV laboratory, Lund. The two datasets for *LsAA9A_Ec* were collected at a wavelength of 0.98 Å and 30% beam transmission for 360° with 0.1° oscillation. One dataset was collected for *TaAA9A* at a wavelength of 0.95 Å and 40% beam transmission for 360° with 0.1° oscillation.

All the three datasets were automatically processed through the EDNA pipeline [48] at the beamline, and were used for further structure determination (Table 1). Both the datasets for *LsAA9A_Ec* extended to a resolution of 1.09 Å, while *TaAA9A* data extended to a resolution of 1.06 Å.

The structure of *LsAA9A_Ec* has been previously determined in the lab (PDB ID: 7PQR) in the space group $P4_1$. The structure of *LsAA9A_Ec_1* is isomorphous to this initial structure. Therefore, its structure was determined by direct refinement of the starting model (7PQR) rigid body and restrained refinement in REFMAC5 [49] of the CCP4 suite [50] along with subsequent model building in COOT [51] and final anisotropic refinement. The structure of *LsAA9A_Ec_2* was instead determined by molecular replacement with the initial model using MOLREP [52] of the CCP4 suite, followed by rigid body and restrained refinement by REFMAC5 and manual model building by COOT. This difference arises because *LsAA9A_Ec* crystallizes in the $P4_1$ space group and can be indexed in 2 non-equivalent indexing with the same cell, and by chance, the EDNA processing pipeline chose the alternate indexing to the one used for the original structure. The dataset for *TaAA9A* was isomorphous to the previously determined structure (PDB ID: 2YET) and its structure was determined by refinement in REFMAC5 and COOT with final anisotropic refinement. The quality of the structures were validated by checking the Ramachandran statistics using RAMPAGE [53] of CCP4 and through the PDB validation (Table 1). The coordinates for *LsAA9A_Ec_2* and *TaAA9A* have been deposited in the PDB with accession codes 7PTZ and 7PU1, respectively. The figures of active sites were prepared in PyMOL 2.0.4 [54].

2.3. Re-Refinement of Other Structures from PDB

Four high resolution LPMO processed data sets and structures (PDB IDs: 5O2X, 4EIR, 5OPF, and 4QI8) were obtained from the PDB (Table 2). All of these structures have the conserved His in the 2nd co-ordination sphere and have resolutions higher than 1.1 Å [35,45,55,56].

2.4. Determination of His Protonation

Geometry of the His imidazole rings were studied as described by Malinska et al., 2015, where the four most sensitive stereochemical parameters in a His ring were used to derive two functions to determine the protonation states of the N atom in the imidazole ring of His [44]. These parameters are the bond lengths $N\delta1-C\epsilon1$ ($X1$ Å) and $C\epsilon1-N\epsilon2$ ($X2$ Å) and the endocyclic angles $-N\delta1-$ ($X3$ degrees) and $-N\epsilon2-$ ($X4$ degrees). The different protonation states are drawn in Figure 3.

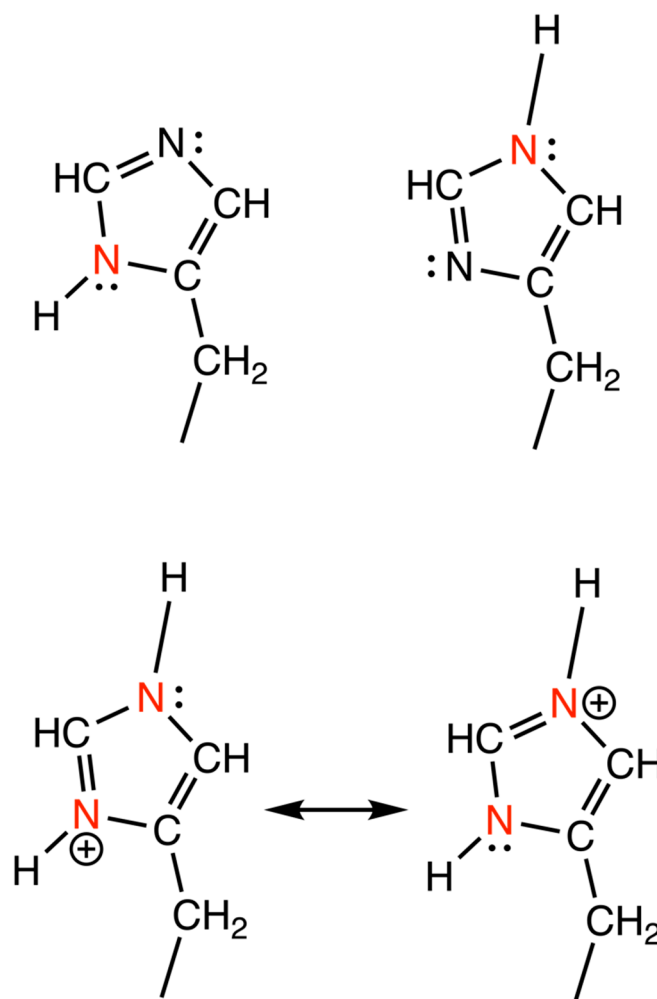


Figure 3. Protonated states of the imidazole ring of histidine side-chain. The top panel represents the singly protonated states with Nδ1 protonated in the left figure and Nε2 protonated in the right. The bottom panel represents the resonance forms of the doubly protonated state. All the protonated nitrogen atoms are colored in red. The figure was prepared using ChemDraw. The doubly deprotonated state is not physiologically relevant due to a pK_a of 14.5, hence not included in these structures.

The functions derived from these parameters are:

$$his1 = -37.31X1 + 15.57X2 - 0.64X3 + 0.76X4 + 17.30 \quad (1)$$

$$his2 = -2.16X1 - 6.08X2 + 0.56X3 + 0.42X4 - 94.46 \quad (2)$$

If the equation $his1$ is negative, only Nδ1 atom of the His ring is protonated. If the equation $his1$ is positive, the value of $his2$ is analyzed. If $his2$ is negative, then, only Nε2 atom of the His ring is protonated. On the other hand, if $his2$ is also positive, both the N atoms are assumed to be protonated. The doubly deprotonated state is excluded from our study as its pK_a is around 14.5 [57].

This study investigates the protonation state of the His in the 2nd co-ordination sphere. To prove the validity of our analysis, the two His residues of the His-brace have also been studied. His1 in the structures of *TaAA9A* and PDBs 5O2X, and 4EIR are methylated as they are expressed in a filamentous fungal host. Therefore, they are excluded from our analysis.

The pK_a values of these histidine residues were calculated for comparison with the experimental results at the crystallization pH using PROPKA v 3.0.4 [58,59] and is listed in Table 3.

2.5. Refinement to Investigate Protonation

All the refinement programs used for protein structure determination including REFMAC5 of CCP4 have a built-in restraint target libraries. For His, these programs always consider it in a doubly protonated state during refinement. In order to investigate the protonation state of the nitrogen atoms in the His ring, it is important to remove the restraints for only the His residues studied in the structure. Thus in this work, restrained refinements were carried out on the structures using REFMAC scripts via command line in a Linux terminal, which allows greater control for restraining the residues. Two independent parallel refinements were carried out: (1) anisotropic restrained refinement for the whole structure, and (2) unrestrained refinement for the three His residues (two in cases where His1 is methylated) under investigation and anisotropic restrained refinement for the rest of the structure. While the 2nd type of refinement is the key protocol for determining the protonation state of His in this study, the former is carried out for comparisons of refinement statistics or changes in geometry. REFMAC scripts were customized to run these refinements. Due to the very high resolution of the structures, the R_{work} and R_{free} were well within acceptable limits. However, in order to ensure that the refinements have been carried out consistently, RMSD bond length of about 0.01–0.02 Å was used as a guiding reference by changing the variable, ‘weighing matrix’ to achieve this. In order to exclude restraints from a particular residue (His1 in the following case), the REFMAC script included the command: RESTRAINT EXCLUDE RESIDUE FROM 1 A TO 1 A ATOMS *. Evaluating the values of *his1* and *his2* functions for the structures where the His-only unrestrained refinement was carried out, will enable us to accurately determine the protonation states of these residues in the structure. NCS restraints were imposed for structures with two molecules in the asymmetric unit. The four geometric parameters of the imidazole ring of the histidines in the refined structures were measured in COOT.

In order to check that His-unrestrained refinement did not result in unreasonable geometry and/or unreasonable B factors average, atomic B factors for the His residues were compared to those of the whole structure in both restrained and His-only-unrestrained refinements using B AVERAGE of CCP4.

3. Results

Our present study aims to investigate the protonation state of the His at the 2nd coordination sphere from the AA9 LPMO structures. Here, the geometry of the His imidazole rings after partial unrestrained refinement were used to derive two functions (*his1/his2*) to determine the protonation states of the N atom.

Six AA9A structures and one AA10 structure (containing the conserved His) with resolutions higher than 1.1 Å were used in this investigation. Three out of the six high resolution AA9A structures, two from *Lentinus similis* (two different data sets for the same enzyme) and one from *Thermoascus aurantiacus*, were determined in this study. Table 1 outlines the data collection and refinement statistics for these three structures.

The data for all the three structures extends to very high resolutions. Although the completeness is low in the highest resolution shells, the $CC_{1/2}$ suggests that inclusion of these data will positively contribute to refinement. In *LsAA9A_Ec_1*, the completeness of the data cutting at resolutions of 1.09 Å and 1.16 Å are 84.6% and 99.8%, respectively. In *LsAA9A_Ec_2*, the completeness of the data cutting at resolutions of 1.09 Å and 1.16 Å are 59.7% and 88.6%, respectively. In *TaAA9A*, the completeness of the data cutting at resolutions of 1.06 Å and 1.2 Å are 40.4% and 94.6%, respectively. Thus, all three datasets have good completeness beyond the threshold of 1.2 Å considered necessary for partial unrestrained refined, and therefore, we decided to extend the datasets to include higher resolutions, which can still contribute to improving the data/parameter ratio in refinement.

His147 in *LsAA9A* and His164 in *TaAA9A* were investigated for the protonation states at N δ 1 and N ϵ 2 atoms of the imidazole ring of the histidines. The analysis was extended to the histidines at the active sites, where it is easy to conclude the protonation state of the imidazole ring, as one atom for each His was coordinated to the Cu ion.

Table 1. Data Collection and Refinement Statistics for the three high resolution structures determined.

	<i>LsAA9A_Ec_1</i>	<i>LsAA9A_Ec_2</i>	<i>TaAA9A</i>
Beamline	BioMAX, MAXIV, Lund	BioMAX, MAXIV, Lund	BioMAX, MAXIV, Lund
Wavelength [Å]	0.9762	0.9762	0.9538 Å
Space group	<i>P</i> 4 ₁	<i>P</i> 4 ₁	<i>P</i> 2 ₁
No. of mols/asymmetric unit	1	1	2
Cell parameters			
(a, b, c) [Å]	48.47, 48.47, 109.72	48.66, 48.66, 109.59	37.65, 89.05, 70.47
(α, β, γ) [°]	90.0	90.0	90.0, 103.3, 90.0
Resolution [Å]	48.5–1.09 (1.15–1.09) *	48.7–1.09 (1.16–1.09)	68.6–1.06 (1.12–1.06)
Completeness [%]	97.2 (84.6)	91.3 (59.7)	84.2 (40.4)
R _{meas} [%]	5.3 (36.1)	5.9 (113.4)	5.4 (43.4)
I/σ(I)	7.21 (3.37)	19.3 (1.5)	18.6 (3.6)
CC _{1/2} [%]	99.8 (88.6)	99.9 (73.1)	99.9 (89.4)
Unique reflections	102,068 (15,109)	96,541 (10,733)	171,807 (12,525)
Observed reflections	1,163,180 (71,657)	1,157,797 (63,079)	1,126,749 (54,423)
Redundancy	11.4 (4.7)	12.0 (5.9)	6.6 (4.3)
No. mol./ASU	1	1	2
R _{work} [%]	11.23	12.35	11.73
R _{free} [%]	12.75	13.93	14.00
RMSD			
Bond lengths [Å]	0.0191	0.0196	0.0193
Bond Angles [°]	2.1238	2.0322	2.3041
Ramachandran Statistics (%)			
Favored	94.8	94.8	98.4
Allowed	5.2	5.2	1.1
Outlier	0.0	0.0	0.4

* Highest resolution shell shown in parenthesis.

The comprehensive set of stereochemical restraint target values and their variances for proteins, EH99 [60] is used in all the refinement programs available in crystallographic structure determination suites. EH99 automatically assigns a double protonation state to histidine, whereby both the nitrogen atoms, Nδ1 and Nε2 have a covalently linked hydrogen atom. Therefore, to determine the true protonation state, it is essential to remove the geometric restraints from the histidine residues to be studied and carry out a specific type of refinement as described above in Section 2.5. Here, the His residues (of the primary and secondary coordination spheres) undergo unrestrained refinement, while the residues in the rest of the structure undergo restrained refinement. This His-only unrestrained refinement should allow these residues to assume the native geometry, if the data is of sufficient quality. The refinement statistics after His-only-unrestrained refinement are listed in Table 2. The values are very similar to completely restrained refinement statistics showing that un-restraining the histidines did not affect the geometry of the overall structure.

The four geometrical parameters of the His ring were measured and the *his1* and *his2* functions calculated. These calculations are tabulated in Table 3.

For the His brace residues, one N-atom is coordinated to the Cu and cannot be protonated. The first His is excluded in those cases where it is methylated. If non-methylated, only its Nε2 atom can be protonated. For the secondary active site His, only Nδ1 can be protonated. To address the deviations from the expected results for the active site residues, the *his1* and *his2* values have been analyzed for the confidence level in predicting protonation. Furthermore, the average B-factors of the overall protein structure and the individual His residues from the parallel restrained and His-only unrestrained refinements have been compared in Table 4.

Table 2. Refinement statistics after restrained and His-unrestrained refinement of the seven structures in this study.

	Crystallization Condition	No. of Mols/Asymmetric Unit	Resolution (Å)	Restrained Refinement	Histidine-Unrestrained Refinement		
				Final R _{Work} /R _{Free} [%]	Final R _{Work} /R _{Free} [%]	Final RMSD Bond lengths [Å]	Final RMSD Bond Angles [°]
LsAA9A_Ec_1	0.1 M citric acid pH 3.5 and 3.0 M NaCl	1	1.09	11.04/12.36	11.39/12.82	0.0131	1.8818
LsAA9A_Ec_2	0.1 M citric acid pH 3.5 and 3.0 M NaCl	1	1.09	12.16/13.79	12.62/13.93	0.0170	1.9397
TaAA9A	0.2 M MgCl ₂ , 0.1 M HEPES pH 7.5, 22% polyacrylic acid	2	1.06	11.94/14.17	11.80/12.70	0.0121	2.0481
5O2X	1.6 M ammonium sulfate, 0.1 M citric acid 4.0	1	0.95	11.29/12.53	11.39/12.58	0.0139	1.9586
4EIR	20% PEG 3350, pH 6.7	2	1.10	12.07/13.52	11.20/12.73	0.0147	1.8145
5OPF	0.04 M potassium phosphate monobasic, 16% w/v PEG8000, 20% v/v glycerol	1	1.08	11.49/13.86	11.79/14.02	0.0124	1.7270
4QI8	0.2M ammonium nitrate, 20% (w/v) PEG 3350, pH 7.0	2	1.10	11.98/14.60	12.08/14.62	0.0161	1.8468

Table 3. Geometrical parameters and estimation of protonation state after His-only unrestrained refinement. The PROPKA predicted pKa values for these histidine residues are also given in the last column. These pKa values denotes the transition of the His imidazole ring from doubly protonated, positively charged state to singly protonated neutral form. The grey boxes represent values of his1 or his2 between +1 and −1, and thus with low confidence in predicting the protonation states. For each structure, the first two (or one in some cases) represent the active site His residues and the last residue represents the 2nd coordination sphere His.

	Nδ1-Cε1 (X ₁) (Å)	Cε1-Nε2 (X ₂) (Å)	-Nδ1-(X ₃) (deg)	-Nε2-(X ₄) (deg)	his1	his2	Protonated Group	Predicted pKa
LsAA9A_Ec_1								
1	1.37	1.33	105.04	108.92	2.3922	−0.9368	Nε2	5.65
78	1.34	1.31	107.76	106.57	−0.3255	−0.2142	Nδ1	3.70
147	1.35	1.37	107.88	110.02	2.7804	0.9156	Nδ1 + Nε2	5.07
LsAA9A_Ec_2								
1	1.36	1.33	105.33	107.53	1.5237	−1.3366	Nε2	5.53
78	1.33	1.37	110.10	106.26	−0.751	0.6228	Nδ1	3.49
147	1.34	1.43	107.53	107.20	2.1689	−0.808	Nε2	4.95
TaAA9A_A chain								
86	1.39	1.33	105.37	105.03	−1.5224	−2.429	Nδ1	2.78
164	1.32	1.33	105.30	109.14	4.2605	−0.5908	Nε2	4.80
TaAA9A_B chain								
86	1.40	1.31	104.16	106.83	−0.0649	−2.2506	Nδ1	2.83
164	1.31	1.33	106.09	107.37	2.7832	−0.8702	Nε2	4.82
5O2X								
86	1.36	1.30	105.81	103.08	−2.6326	−2.7544	Nδ1	2.45
163	1.34	1.34	105.72	107.36	2.0476	−1.2072	Nε2	4.63
4EIR_A chain								
84	1.35	1.30	107.34	106.85	−0.3731	−0.2926	Nδ1	2.21
157	1.30	1.32	106.39	108.31	3.5234	−0.225	Nε2	4.68
4EIR_B chain								
84	1.33	1.32	108.83	105.27	−1.4691	−0.2002	Nδ1	2.24
157	1.31	1.33	106.17	107.73	3.0056	−0.6742	Nε2	4.67
5OPF								
37	1.33	1.32	105.02	103.23	−0.5811	−3.1906	Nδ1	3.44
144	1.32	1.30	106.03	103.60	−0.8842	−2.3264	Nδ1	2.18
216	1.30	1.34	103.87	104.49	2.5444	−3.3622	Nε2	4.83
4QI8_A chain								
1	1.36	1.28	105.25	110.2	2.8256	0.044	Nδ1 + Nε2	4.29
72	1.34	1.30	107.14	104.41	−1.7260	−1.4078	Nδ1	2.19
146	1.33	1.36	105.18	105.13	1.3833	−2.5462	Nε2	4.75
4QI8_B chain								
1	1.37	1.32	106.58	107.07	−0.1551	−0.7906	Nδ1	4.23
72	1.36	1.32	107.96	105.84	−1.5996	−0.5128	Nδ1	2.11
146	1.32	1.32	105.02	106.52	2.2928	−1.7872	Nε2	4.64

Table 4. Average B factors for overall protein structure and the His residues after restrained and His-only restrained refinement.

Histidine Residue Number in This Study	B _{average} (Å ²) from Restrained Refinement	B _{average} (Å ²) from His-Only Unrestrained Refinement
<i>LsAA9A_Ec_1</i>		
Overall_protein-chain	14.1	14.1
1	12.7	12.8
78	13.1	13.1
147	14.1	14.2
<i>LsAA9A_Ec_2</i>		
Overall_protein-chain	17.5	17.7
1	15.7	15.8
78	15.8	15.9
147	17.5	17.7
<i>TaAA9A</i>		
Overall_protein-chainA	12.5	12.3
86_chainA	9.4	9.4
164_chainA	10.0	10.0
Overall_protein-chainB	12.9	12.8
86_chainB	9.8	9.7
164_chainB	10.7	10.7
5O2X		
Overall_protein	7.1	7.0
86	5.8	5.7
163	6.8	6.8
4EIR		
Overall_protein-chainA	17.8	16.9
84_chainA	12.7	12.6
157_chainA	14.1	14.0
Overall_protein-chainB	13.1	12.8
84_chainB	10.8	10.7
157_chainB	11.4	11.4
5OPF		
Overall_protein	9.4	9.3
37	8.0	8.0
144	7.2	7.1
216	7.8	7.8
4QI8		
Overall_protein-chainA	17.8	16.9
1_chainA	10.7	10.6
72_chainA	27.1	26.5
146_chainA	13.5	13.4
Overall_protein-chainB	13.0	12.8
1_chainB	10.2	10.2
72_chainB	28.4	27.3
146_chainB	12.4	12.3

The comparable values imply that removing the restraints from the histidines did not distort the geometry of the protein structure around these residues, thereby increasing the confidence level of our analysis. In all the cases, where there is an incorrect assignment of the protonated group for the His-brace residues, the values of *his1* and *his2* are found to be too low for correct estimation. Malinska and coworkers suggest that the protonation state for Nδ1 can be predicted with high probability when *his1* is less than -1.0 . Similarly, the protonation state for Nε2 can be predicted with high probability if *his1* is positive and the *his2* is less than -1.0 [44]. Our results suggest that the His of the secondary coordination sphere is singly protonated at the Nε2 atom in most if not all structures. The results from our calculations and the predicted protonation sites are shown in Figure 4. For comparison, the structure of *LsAA9A_Ao* expressed in *Aspergillus oryzae* (PDB id: 5ACG)

was superposed on *LsAA9A_Ec_2* structure after its His-only unrestrained refinement, also showing the presence of the two water molecules.

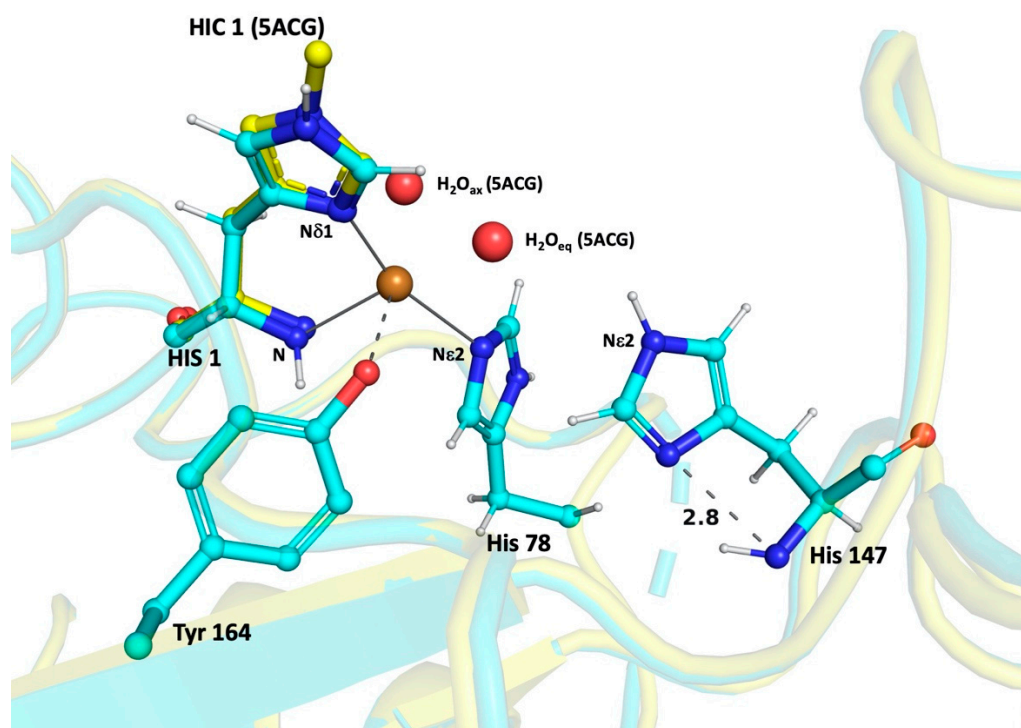


Figure 4. Results from His-only unrestrained refinement in *LsAA9A_Ec_2* structure (cyan colored). His147 shows single protonation N ϵ 2 atom. The His-brace residues (internal control) show their single protonation state. The H-bond distance between the N δ 1 and backbone N atoms of His147 is shown in Å. The structure of *LsAA9A_Ao* (PDB id: 5ACG, yellow colored) is shown for comparison with 1st His methylated (HIC) and the two water molecules bound to the Cu(II). The oxygen species binds at the position of H₂O_{eq}. The figure was prepared with Pymol.

4. Discussion

In the AA9 LPMO family, a conserved histidine in the secondary coordination sphere has been proposed, among other roles, to donate proton to the oxygen species via the N ϵ 2 of its imidazole ring [31,32]. The present study was carried out to experimentally determine the protonation state of this conserved His residue using high resolution AA9 LPMO X-ray crystal structures, thereby adding experimental information to discussion of its role in proton transfer and a better starting basis for computational studies.

X-ray crystallography is a powerful tool for determining atomic resolution structures of proteins. X-rays can accurately determine the positions for almost all the atoms. Unfortunately, the hydrogen atom, being the lightest atom with one electron, has a very low scattering factor and the electron density is localized in the bond. Therefore, it is difficult to determine its position using this technique in the resolution ranges observed for proteins. However, it has been suggested that for structures with resolutions higher than 1.2 Å, the position of the hydrogen atoms can be predicted with a certain level of accuracy in protein structures [44]. We were able to carry out this study on seven different high resolution LPMO structures, which enabled us to validate our results across different enzymes within the AA9 family, as well as one AA10 enzyme.

To evaluate the accuracy of the prediction of this analysis, protonation states for the active site His were also deduced. These histidines can only be singly protonated as one of the N atom (N δ 1 of His1 and N ϵ 2 of the second His residue in the His-brace) is coordinated to Cu. There were four deviations from the expected protonation. These are His147 of *LsAA9A_Ec_1* (*his2* = 0.9156), His37 of the PDB structure 5OPF (*his1* = −0.5811), and His1

of both chains A ($his2 = 0.044$) and B ($his1 = -0.1551$) in the PDB structure 4QI8. The last three deviations are below the high confidence threshold, and with these exceptions the protonation states of all His-brace residues were accurately deduced from this study. This increases the confidence in our result on the secondary co-ordination sphere His which show that only N ϵ 2 is protonated, while N δ 1 is in the deprotonated state. The only exception is *LsAA9A_Ec_1* structure, which shows protonation at both N δ 1 and N ϵ 2 atoms, though with low confidence (as shown in Table 3). Examination of the micro-environment of this His residue in all the LPMO structures of this study show also that the distance of the N δ 1 atom from main chain N-H is between 2.75 to 2.95 Å. Therefore, this N is likely to serve as a H-bond acceptor and reinforcing the view that the His is unlikely to be doubly protonated.

From our study, where we observe only the single protonation of the conserved 2nd coordination sphere His at the N ϵ 2 atom, we can conclude that this His will not be able to act as a proton donor to the oxygen species. Computational studies on *LsAA9A* have also shown that the H₂O₂ co-substrate does not require proton transfer (and thus double protonation) [27,33]. A new experimental study further highlights that H₂O₂ is the co-substrate strictly required for *LsAA9A* glycosidic bond cleavage activity [28]. Thus, at least for *LsAA9A* there is currently no evidence of His147 double protonation or proton transfer being necessary for the mechanism.

In neutron crystallography experiments on *Neurospora crassa* LPMO only N ϵ 2 atom of this second co-ordination sphere His is found to be protonated [32], though it was suggested the residue might be deprotonated in the active form at lower pH.

Table 3 shows the pH of the crystallization condition for all the structures used in this study, which range from 3.5–7.5. Though there might be deviation from the nominal crystallization pH, the pH range suggests that in spite of the crystallization conditions being acidic for some cases, it does not change the protonation state of the LPMO. Based on our PROPKA calculations in Table 3, the pK_a of the 2nd coordination sphere His is in the range of 4.64–5.07, which shows that it will be neutral at the pH of 6.0–7.0, where LPMO activity is often measured. This also implies that for the structures in this study, where crystallization pH is very low, we would expect some doubly protonated state, which might be what the low confidence doubly protonated state of the *LsAA9A_Ec_1* structure shows. As all other structures though generally show single protonation, it is likely that the pK_a s of this His might be even lower than those predicted by PROPKA.

Taken together, our study using partial unrestrained refinement of high-resolution LPMO structures shows that the secondary co-ordination sphere His is primarily singly protonated at N ϵ 2 atom at all crystallization conditions and pH, arguing against a general role as proton donor, as the most recent computational studies also suggest. However, the possibility that the presence of the oxygen species/saccharide substrate brings changes in the His pK_a directly or through structural changes cannot be completely excluded, and neither is the possibility that this doubly protonated species is transient and thus not possible to characterize by X-ray crystallography.

In conclusion, the scope of this study was to probe into the protonation state of a specific His residue. Based on our internal validation using the His-brace, the *his1/his2* assignments are highly reliable (except those in low confidence zone). More and more X-ray structures of enzymes are being determined to better than 1.2 Å resolution, and the role of His in catalysis is widespread in many types of enzymes. Thus, based on the current experience with LPMOs, we recommend the use of the partial restrained protocol devised by [44] as a complement to neutron crystallography in order to determine experimentally the protonation state of important histidines.

Author Contributions: Conceptualization, L.L.L.; methodology, L.L.L. and S.B.; validation, S.B.; formal analysis, L.L.L. and S.B.; investigation, S.B.; resources, K.E.H.F., S.J.M., T.T., R.K.S., J.Ø.I. and C.H.-R.; writing—original draft preparation, L.L.L. and S.B.; writing—review and editing, all authors; visualization, S.B.; supervision, L.L.L., M.J.B., K.S.J. and M.H.H.N.; project administration, L.L.L.; funding acquisition, L.L.L., K.S.J., M.J.B. and M.H.H.N. All authors have read and agreed to the published version of the manuscript.

Funding: This study was funded by the Novo Nordisk Foundation HOPE project (NNF17SA0027704), Novo Nordisk Foundation project “Harnessing the Energy of the Sun for Biomass Conversion” (NNF16OC0021832) and the Danish Council for Independent Research (grant number 8021-00273B). Synchrotron trips was supported by the Danish Ministry of Higher Education and Science through the Instrument Center DANSCATT. S.B., S.J.M., T.T., M.J.B. and L.L.L. are members of ISBUC, Integrative Structural Biology at the University of Copenhagen (www.isbuc.ku.dk, 17 January 2022).

Institutional Review Board Statement: Not applicable.

Informed Consent Statement: Not applicable.

Data Availability Statement: Publicly available datasets were analyzed in this study. These data can be found here: <https://www.rcsb.org>, 17 January 2022. New PDB datasets from this study are 7PTZ and 7PU1.

Acknowledgments: The authors thank Novozymes A/S for providing the TaAA9A protein sample. The authors acknowledge MAX IV Laboratory for time on beam line BioMAX [61] under Proposal 20190334 and 20200120. Research conducted at MAX IV, a Swedish national user facility, is supported by the Swedish Research council under contract 2018-07152, the Swedish Governmental Agency for Innovation Systems under contract 2018-04969, and Formas under contract 2019-02496. We thank Ana Gonzalez with the remote data collection on the beamline for the datasets used in this paper. We thank Kira Devantier and Cecilie R. Oksbjerg for initial tests and Mohannad Aloula for assistance in crystallization.

Conflicts of Interest: The authors declare that they have no conflict of interest. The funders had no role in the design of the study; in the collection, analyses, or interpretation of data; in the writing of the manuscript, or in the decision to publish the results.

References

1. Horn, S.; Vaaje-Kolstad, G.; Westereng, B.; Eijsink, V.G. Novel enzymes for the degradation of cellulose. *Biotechnol. Biofuels* **2012**, *5*, 45. [[CrossRef](#)] [[PubMed](#)]
2. Lo Leggio, L.; Simmons, T.J.; Poulsen, J.-C.N.; Frandsen, K.E.H.; Hemsworth, G.R.; Stringer, M.A.; von Freiesleben, P.; Tovborg, M.; Johansen, K.S.; De Maria, L.; et al. Structure and boosting activity of a starch-degrading lytic polysaccharide monoxygenase. *Nat. Commun.* **2015**, *6*, 5961. [[CrossRef](#)] [[PubMed](#)]
3. Harris, P.V.; Welner, D.; McFarland, K.C.; Re, E.; Navarro Poulsen, J.-C.; Brown, K.; Salbo, R.; Ding, H.; Vlasenko, E.; Merino, S.; et al. Stimulation of Lignocellulosic Biomass Hydrolysis by Proteins of Glycoside Hydrolase Family 61: Structure and Function of a Large, Enigmatic Family. *Biochemistry* **2010**, *49*, 3305–3316. [[CrossRef](#)] [[PubMed](#)]
4. Müller, G.; Várnai, A.; Johansen, K.S.; Eijsink, V.G.H.; Horn, S.J. Harnessing the potential of LPMO-containing cellulase cocktails poses new demands on processing conditions. *Biotechnol. Biofuels* **2015**, *8*, 187. [[CrossRef](#)]
5. Himmel, M.E.; Ding, S.-Y.; Johnson, D.K.; Adney, W.S.; Nimlos, M.R.; Brady, J.W.; Foust, T.D. Biomass Recalcitrance: Engineering Plants and Enzymes for Biofuels Production. *Science* **2007**, *315*, 804–807. [[CrossRef](#)]
6. Sheldon, R.A. Green and sustainable manufacture of chemicals from biomass: State of the art. *Green Chem.* **2014**, *16*, 950–963. [[CrossRef](#)]
7. Johansen, K.S. Discovery and industrial applications of lytic polysaccharide mono-oxygenases. *Biochem. Soc. Trans.* **2016**, *44*, 143–149. [[CrossRef](#)]
8. Shah, F.; Nicolás, C.; Bentzer, J.; Ellström, M.; Smits, M.; Rineau, F.; Canbäck, B.; Floudas, D.; Carleer, R.; Lackner, G.; et al. Ectomycorrhizal fungi decompose soil organic matter using oxidative mechanisms adapted from saprotrophic ancestors. *New Phytol.* **2016**, *209*, 1705–1719. [[CrossRef](#)]
9. Blanco-Ulate, B.; Morales-Cruz, A.; Amrine, K.C.H.; Labavitch, J.M.; Powell, A.L.T.; Cantu, D. Genome-wide transcriptional profiling of *Botrytis cinerea* genes targeting plant cell walls during infections of different hosts. *Front. Plant Sci.* **2014**, *5*, 435. [[CrossRef](#)]
10. Askarian, F.; Uchiyama, S.; Masson, H.; Sørensen, H.V.; Golten, O.; Bunæs, A.C.; Mekasha, S.; Røhr, Å.K.; Kommedal, E.; Ludviksen, J.A.; et al. The lytic polysaccharide monoxygenase CbpD promotes *Pseudomonas aeruginosa* virulence in systemic infection. *Nat. Commun.* **2021**, *12*, 1230. [[CrossRef](#)]

11. Lombard, V.; Golaconda Ramulu, H.; Drula, E.; Coutinho, P.M.; Henrissat, B. The carbohydrate-active enzymes database (CAZy) in 2013. *Nucleic Acids Res.* **2014**, *42*, D490–D495. [[CrossRef](#)] [[PubMed](#)]
12. Tandrup, T.; Frandsen, K.E.H.; Johansen, K.S.; Berrin, J.-G.; Lo Leggio, L. Recent insights into lytic polysaccharide monoxygenases (LPMOs). *Biochem. Soc. Trans.* **2018**, *46*, 1431–1447. [[CrossRef](#)] [[PubMed](#)]
13. Vu, V.V.; Ngo, S.T. Copper active site in polysaccharide monoxygenases. *Coord. Chem. Rev.* **2018**, *368*, 134–157. [[CrossRef](#)]
14. Wang, B.; Wang, Z.; Davies, G.J.; Walton, P.H.; Rovira, C. Activation of O₂ and H₂O₂ by Lytic Polysaccharide Monoxygenases. *ACS Catal.* **2020**, *10*, 12760–12769. [[CrossRef](#)]
15. Eijsink, V.G.H.; Petrovic, D.; Forsberg, Z.; Mekasha, S.; Røhr, Å.K.; Várnai, A.; Bissaro, B.; Vaaje-Kolstad, G. On the functional characterization of lytic polysaccharide monoxygenases (LPMOs). *Biotechnol. Biofuels* **2019**, *12*, 58. [[CrossRef](#)] [[PubMed](#)]
16. Quinlan, R.J.; Sweeney, M.D.; Lo Leggio, L.; Otten, H.; Poulsen, J.-C.N.; Johansen, K.S.; Krogh, K.B.R.M.; Jorgensen, C.I.; Tovborg, M.; Anthonsen, A.; et al. Insights into the oxidative degradation of cellulose by a copper metalloenzyme that exploits biomass components. *Proc. Natl. Acad. Sci. USA* **2011**, *108*, 15079–15084. [[CrossRef](#)] [[PubMed](#)]
17. Sabbadin, F.; Urresti, S.; Henrissat, B.; Avrova, A.O.; Welsh, L.R.J.; Lindley, P.J.; Csukai, M.; Squires, J.N.; Walton, P.H.; Davies, G.J.; et al. Secreted pectin monoxygenases drive plant infection by pathogenic oomycetes. *Science* **2021**, *373*, 774–779. [[CrossRef](#)]
18. Frandsen, K.E.H.; Simmons, T.J.; Dupree, P.; Poulsen, J.-C.N.; Hemsworth, G.R.; Ciano, L.; Johnston, E.M.; Tovborg, M.; Johansen, K.S.; von Freiesleben, P.; et al. The molecular basis of polysaccharide cleavage by lytic polysaccharide monoxygenases. *Nat. Chem. Biol.* **2016**, *12*, 298–303. [[CrossRef](#)]
19. Frandsen, K.E.H.; Lo Leggio, L. Lytic polysaccharide monoxygenases: A crystallographer's view on a new class of biomass-degrading enzymes. *IUCr* **2016**, *3*, 448–467. [[CrossRef](#)]
20. Vaaje-Kolstad, G.; Westereng, B.; Horn, S.J.; Liu, Z.; Zhai, H.; Sørli, M.; Eijsink, V.G.H. An Oxidative Enzyme Boosting the Enzymatic Conversion of Recalcitrant Polysaccharides. *Science* **2010**, *330*, 219–222. [[CrossRef](#)]
21. Langston, J.A.; Shaghasi, T.; Abbate, E.; Xu, F.; Vlasenko, E.; Sweeney, M.D. Oxidoreductive Cellulose Depolymerization by the Enzymes Cellobiose Dehydrogenase and Glycoside Hydrolase 61. *Appl. Environ. Microbiol.* **2011**, *77*, 7007–7015. [[CrossRef](#)]
22. Fushinobu, S. A new face for biomass breakdown. *Nat. Chem. Biol.* **2014**, *10*, 88–89. [[CrossRef](#)]
23. Westereng, B.; Cannella, D.; Wittrup Agger, J.; Jørgensen, H.; Larsen Andersen, M.; Eijsink, V.G.H.; Felby, C. Enzymatic cellulose oxidation is linked to lignin by long-range electron transfer. *Sci. Rep.* **2015**, *5*, 18561. [[CrossRef](#)] [[PubMed](#)]
24. Kracher, D.; Andlar, M.; Furtmüller, P.G.; Ludwig, R. Active-site copper reduction promotes substrate binding of fungal lytic polysaccharide monoxygenase and reduces stability. *J. Biol. Chem.* **2018**, *293*, 1676–1687. [[CrossRef](#)]
25. Hangasky, J.A.; Iavarone, A.T.; Marletta, M.A. Reactivity of O₂ versus H₂O₂ with polysaccharide monoxygenases. *Proc. Natl. Acad. Sci. USA* **2018**, *115*, 4915–4920. [[CrossRef](#)] [[PubMed](#)]
26. Bissaro, B.; Røhr, Å.K.; Müller, G.; Chylenski, P.; Skaugen, M.; Forsberg, Z.; Horn, S.J.; Vaaje-Kolstad, G.; Eijsink, V.G.H. Oxidative cleavage of polysaccharides by monocopper enzymes depends on H₂O₂. *Nat. Chem. Biol.* **2017**, *13*, 1123–1128. [[CrossRef](#)]
27. Hedegård, E.D.; Ryde, U. Molecular mechanism of lytic polysaccharide monoxygenases. *Chem. Sci.* **2018**, *9*, 3866–3880. [[CrossRef](#)]
28. Brander, S.; Tokin, R.; Ipsen, J.Ø.; Jensen, P.E.; Hernández-Rollán, C.; Nørholm, M.H.H.; Lo Leggio, L.; Dupree, P.; Johansen, K.S. Scission of Glucosidic Bonds by a *Lentinus similis* Lytic Polysaccharide Monoxygenases Is Strictly Dependent on H₂O₂ while the Oxidation of Saccharide Products Depends on O₂. *ACS Catal.* **2021**, *11*, 13848–13859. [[CrossRef](#)]
29. Shook, R.L.; Borovik, A.S. Role of the secondary coordination sphere in metal-mediated dioxygen activation. *Inorg. Chem.* **2010**, *49*, 3646–3660. [[CrossRef](#)]
30. Holm, R.H.; Kennepohl, P.; Solomon, E.I. Structural and Functional Aspects of Metal Sites in Biology. *Chem. Rev.* **1996**, *96*, 2239–2314. [[CrossRef](#)] [[PubMed](#)]
31. Span, E.A.; Suess, D.L.M.; Deller, M.C.; Britt, R.D.; Marletta, M.A. The Role of the Secondary Coordination Sphere in a Fungal Polysaccharide Monoxygenase. *ACS Chem. Biol.* **2017**, *12*, 1095–1103. [[CrossRef](#)]
32. O'Dell, W.B.; Agarwal, P.K.; Meilleur, F. Oxygen Activation at the Active Site of a Fungal Lytic Polysaccharide Monoxygenase. *Angew. Chem. Int. Ed.* **2017**, *56*, 767–770. [[CrossRef](#)]
33. Wang, B.; Walton, P.H.; Rovira, C. Molecular Mechanisms of Oxygen Activation and Hydrogen Peroxide Formation in Lytic Polysaccharide Monoxygenases. *ACS Catal.* **2019**, *9*, 4958–4969. [[CrossRef](#)]
34. Wu, M.; Beckham, G.T.; Larsson, A.M.; Ishida, T.; Kim, S.; Payne, C.M.; Himmel, M.E.; Crowley, M.F.; Horn, S.J.; Westereng, B.; et al. Crystal Structure and Computational Characterization of the Lytic Polysaccharide Monoxygenase GH61D from the Basidiomycota Fungus *Phanerochaete chrysosporium*. *J. Biol. Chem.* **2013**, *288*, 12828–12839. [[CrossRef](#)]
35. Li, X.; Beeson, W.T.; Phillips, C.M.; Marletta, M.A.; Cate, J.H.D. Structural Basis for Substrate Targeting and Catalysis by Fungal Polysaccharide Monoxygenases. *Structure* **2012**, *20*, 1051–1061. [[CrossRef](#)] [[PubMed](#)]
36. Frericks Schmidt, H.L.; Shah, G.J.; Sperling, L.J.; Rienstra, C.M. NMR Determination of Protein pK_a Values in the Solid State. *J. Phys. Chem. Lett.* **2010**, *1*, 1623–1628. [[CrossRef](#)] [[PubMed](#)]
37. Hansen, A.L.; Kay, L.E. Measurement of histidine pK_a values and tautomer populations in invisible protein states. *Proc. Natl. Acad. Sci. USA* **2014**, *111*, E1705–E1712. [[CrossRef](#)]
38. Wallerstein, J.; Weininger, U.; Khan, M.A.I.; Linse, S.; Akke, M. Site-Specific Protonation Kinetics of Acidic Side Chains in Proteins Determined by pH-Dependent Carboxyl ¹³C NMR Relaxation. *J. Am. Chem. Soc.* **2015**, *137*, 3093–3101. [[CrossRef](#)] [[PubMed](#)]

39. Kneller, D.W.; Phillips, G.; Weiss, K.L.; Pant, S.; Zhang, Q.; O'Neill, H.M.; Coates, L.; Kovalevsky, A. Protonation states in SARS-CoV-2 main protease mapped by neutron crystallography. *bioRxiv* **2020**, bioRxiv: 2020.09.22.308668. [[CrossRef](#)]
40. Wan, Q.; Parks, J.M.; Hanson, B.L.; Fisher, S.Z.; Ostermann, A.; Schrader, T.E.; Graham, D.E.; Coates, L.; Langan, P.; Kovalevsky, A. Direct determination of protonation states and visualization of hydrogen bonding in a glycoside hydrolase with neutron crystallography. *Proc. Natl. Acad. Sci. USA* **2015**, *112*, 12384–12389. [[CrossRef](#)]
41. Zaccai, N.R.; Coquelle, N. Opportunities and challenges in neutron crystallography. *EPJ Web Conf.* **2020**, *236*, 02001. [[CrossRef](#)]
42. Aachmann, F.L.; Sorlie, M.; Skjak-Braek, G.; Eijsink, V.G.H.; Vaaje-Kolstad, G. NMR structure of a lytic polysaccharide monoxygenase provides insight into copper binding, protein dynamics, and substrate interactions. *Proc. Natl. Acad. Sci. USA* **2012**, *109*, 18779–18784. [[CrossRef](#)] [[PubMed](#)]
43. Madland, E.; Forsberg, Z.; Wang, Y.; Lindorff-Larsen, K.; Niebisch, A.; Modregger, J.; Eijsink, V.G.; Aachmann, F.L.; Courtade, G. NMR structures and functional roles of two related chitin-binding domains of a lytic polysaccharide monoxygenase from *Cellvibrio japonicus*. *BioRxiv* **2021**. [[CrossRef](#)]
44. Malinska, M.; Dauter, M.; Kowiel, M.; Jaskolski, M.; Dauter, Z. Protonation and geometry of histidine rings. *Acta Crystallogr. Sect. D Biol. Crystallogr.* **2015**, *71*, 1444–1454. [[CrossRef](#)]
45. Forsberg, Z.; Bissaro, B.; Gullesen, J.; Dalhus, B.; Vaaje-Kolstad, G.; Eijsink, V.G.H. Structural determinants of bacterial lytic polysaccharide monoxygenase functionality. *J. Biol. Chem.* **2018**, *293*, 1397–1412. [[CrossRef](#)]
46. Hernández-Rollán, C.; Falkenberg, K.B.; Rennig, M.; Bertelsen, A.B.; Ipsen, J.Ø.; Brander, S.; Daley, D.O.; Johansen, K.S.; Nørholm, M.H.H. LyGo: A Platform for Rapid Screening of Lytic Polysaccharide Monoxygenase Production. *ACS Synth. Biol.* **2021**, *10*, 897–906. [[CrossRef](#)] [[PubMed](#)]
47. Singh, R.K.; Blossom, B.M.; Russo, D.A.; van Oort, B.; Croce, R.; Jensen, P.E.; Felby, C.; Bjerrum, M.J. Thermal unfolding and refolding of a lytic polysaccharide monoxygenase from *Thermoascus aurantiacus*. *RSC Adv.* **2019**, *9*, 29734–29742. [[CrossRef](#)]
48. Incardona, M.-F.; Bourenkov, G.P.; Levik, K.; Pieritz, R.A.; Popov, A.N.; Svensson, O. EDNA: A framework for plugin-based applications applied to X-ray experiment online data analysis. *J. Synchrotron Radiat.* **2009**, *16*, 872–879. [[CrossRef](#)]
49. Murshudov, G.N.; Vagin, A.A.; Dodson, E.J. Refinement of Macromolecular Structures by the Maximum-Likelihood Method. *Acta. Crystallogr. Sect. D Biol. Crystallogr.* **1997**, *53*, 240–255. [[CrossRef](#)]
50. Winn, M.D.; Ballard, C.C.; Cowtan, K.D.; Dodson, E.J.; Emsley, P.; Evans, P.R.; Keegan, R.M.; Krissinel, E.B.; Leslie, A.G.W.; McCoy, A.; et al. Overview of the CCP 4 suite and current developments. *Acta. Crystallogr. Sect. D Biol. Crystallogr.* **2011**, *67*, 235–242. [[CrossRef](#)] [[PubMed](#)]
51. Emsley, P.; Cowtan, K. Coot: Model-building tools for molecular graphics. *Acta. Crystallogr. D. Biol. Crystallogr.* **2004**, *60*, 2126–2132. [[CrossRef](#)] [[PubMed](#)]
52. Vagin, A.; Teplyakov, A. MOLREP: An Automated Program for Molecular Replacement. *J. Appl. Crystallogr.* **1997**, *30*, 1022–1025. [[CrossRef](#)]
53. Lovell, S.C.; Davis, I.W.; Arendall, W.B.; de Bakker, P.I.W.; Word, J.M.; Prisant, M.G.; Richardson, J.S.; Richardson, D.C. Structure validation by $C\alpha$ geometry: ϕ , ψ and $C\beta$ deviation. *Proteins Struct. Funct. Bioinforma.* **2003**, *50*, 437–450. [[CrossRef](#)]
54. Schrodinger, L.L.C. The PyMOL Molecular Graphics System, Version 2.0.1 2018. Available online: <https://pymol.org> (accessed on 17 January 2022).
55. Hansson, H.; Karkehabadi, S.; Mikkelsen, N.; Douglas, N.R.; Kim, S.; Lam, A.; Kaper, T.; Kelemen, B.; Meier, K.K.; Jones, S.M.; et al. High-resolution structure of a lytic polysaccharide monoxygenase from *Hypocrea jecorina* reveals a predicted linker as an integral part of the catalytic domain. *J. Biol. Chem.* **2017**, *292*, 19099–19109. [[CrossRef](#)]
56. Tan, T.-C.; Kracher, D.; Gandini, R.; Sygmund, C.; Kittl, R.; Haltrich, D.; Hällberg, B.M.; Ludwig, R.; Divne, C. Structural basis for cellobiose dehydrogenase action during oxidative cellulose degradation. *Nat. Commun.* **2015**, *6*, 7542. [[CrossRef](#)]
57. Eicher, T.; Hauptmann, S.; Speicher, A. *The Chemistry of Heterocycles*; Wiley: Hoboken, NJ, USA, 2003; ISBN 9783527307203.
58. Søndergaard, C.R.; Olsson, M.H.M.; Rostkowski, M.; Jensen, J.H. Improved Treatment of Ligands and Coupling Effects in Empirical Calculation and Rationalization of pK_a Values. *J. Chem. Theory Comput.* **2011**, *7*, 2284–2295. [[CrossRef](#)] [[PubMed](#)]
59. Olsson, M.H.M.; Søndergaard, C.R.; Rostkowski, M.; Jensen, J.H. PROPKA3: Consistent Treatment of Internal and Surface Residues in Empirical pK_a Predictions. *J. Chem. Theory Comput.* **2011**, *7*, 525–537. [[CrossRef](#)]
60. Arnold, E.; Himmel, D.M. *International Tables for Crystallography, Vol. F*; M.G. Kluwer Academic Publishers: New York, NY, USA, 2001; ISBN 978-0-470-66078-2.
61. Ursby, T.; Åhnberg, K.; Appio, R.; Aurelius, O.; Barczyk, A.; Bartalesi, A.; Bjelčić, M.; Bolmsten, F.; Cerenius, Y.; Doak, R.B.; et al. BioMAX—The first macromolecular crystallography beamline at MAX IV Laboratory. *J. Synchrotron Rad.* **2020**, *27*, 1415–1429. [[CrossRef](#)]